DEVELOPMENTAL BIOLOGY

Genetically encoded tension heterogeneity sculpts cardiac trabeculation

Jinxiu Liang[1,2,3], Peijun Jiang[1,2,3], Shuaifang Yan[4], Tao Cheng[1,2,5], Shuo Chen[1,2,3], Kexin Xian[4], Pengfei Xu[1,2,5], Jing-Wei Xiong[6], Aibin He[4], Jia Li[7]*, Peidong Han[1,2,3]*

The myocardial wall arises from a single layer of cardiomyocytes, some delaminate to create trabeculae while others remain in the compact layer. However, the mechanisms governing cardiomyocyte fate decisions remain unclear. Using single-cell RNA sequencing, genetically encoded biosensors, and in toto live imaging, we observe intrinsic variations in *erbb2* expression and its association with trabecular fate. Specifically, *erbb2* promotes PI3K activity and recruits the Arp2/3 complex, inducing a polarized accumulation of the actomyosin network to drive cell delamination. Subsequently, the lineage-committed nascent trabeculae trigger Notch activity in neighboring cardiomyocytes to suppress *erbb2* expression and reduce cell tension, thereby confining them to the compact layer. Overall, this genetic and cellular interplay governs compact and trabecular cell fate determination to orchestrate myocardial pattern formation.

INTRODUCTION

A fundamental question in vertebrate organogenesis is how different cell lineages are spatiotemporally integrated to establish a complex structure (*1*–*3*). In particular, the vertebrate heart initially exists as a heart tube with a single layer of cardiomyocytes, and later, they adopt two distinct fates, with some cells undergoing directional migration to form trabeculae, while others stay in the compact layer (*4*, *5*). The trabeculation sequence is stringently orchestrated to ensure the proportional allocation of cardiomyocytes (*6*), and disruptions in this morphogenesis process result in diverse congenital heart diseases and early lethality (*7*).

Previous studies have enhanced our understanding of the genetic and biomechanical factors involved in cardiac structure formation (*8*, *9*). For example, the Neuregulin (Nrg)–Erbb2 axis is a pivotal signaling pathway regulating trabeculation. Erbb2 lacks the ability to bind Nrg ligands directly; instead, it forms heterodimers with other Erbb receptors, such as Erbb4, to mediate downstream signaling. Deficiency in either Nrg or Erbb2 results in substantial defects in heart development, attributed to compromised proliferation or directional migration of cardiomyocytes (*10*–*13*). Moreover, in the treatment of patients with breast cancer with overactive Erbb2 activity, the use of Erbb2-blocking antibodies often leads to cardiomyopathy (*14*). Collectively, these studies underscore the essential role of this signaling axis in both heart development and functional maintenance.

A recent study has identified cardiomyocyte apical tension as a primary driver in trabecular pattern formation. In their hypothesis, cardiomyocytes carrying high tension delaminate from the single-layered myocardium to generate nascent trabeculae, while cells with low apical tension remain in the compact layer (*15*). However, it remains unclear whether tension heterogeneity occurs in a stochastic manner or is predetermined by genetic factors. Here, we provide evidence that the expression of *erbb2* in a distinct subpopulation of cardiomyocytes directly induces cardiomyocyte tension to initiate the trabecular fate. Our results demonstrate that *erbb2* is differentially expressed in the developing zebrafish heart. Cardiomyocytes with high *erbb2* expression sprout and generate nascent trabeculae, while those with low *erbb2* expression remain in the compact layer. In particular, *erbb2* directly triggers PI3K activity and recruits Arp2/3 complex to induce polarized accumulation of the actomyosin network. Manipulating *erbb2*, cell tension, and Arp2/3 activities at the single-cell level uncovers the cell-autonomous function of *erbb2* in controlling tension, independent of its role in regulating cardiomyocyte proliferation. Therefore, the intricate genetic and cellular interactions mediated by heterogeneous *erbb2* expression play a crucial role in determining compact and trabecular cell fate.

RESULTS

Intrinsic variations in *erbb2* expression in developing zebrafish ventricles

In developing zebrafish embryos, the heart is a single layer at 48 hours postfertilization (hpf), and prominent trabeculae can be observed by 72 hpf. To elucidate the intrinsic gene expression profiles associated with trabeculation, we performed single-cell RNA sequencing on isolated cardiomyocytes (Fig. 1A) and integrated our findings with previously published datasets (*16*). We first reconstructed single-cell transcriptomic maps through unsupervised clustering and annotated these clusters based on their characteristic markers (table S1). Seven cell types were identified (fig. S1, A and B) in 48-hpf hearts, including ventricular cardiomyocytes (CM-Vs), atrial cardiomyocytes (CM-As), endocardial cells (ECs), immune cells (ICs), epicardial cells (EPs), erythrocytes (RBCs), and fibroblasts (FBs). *erbb2*, which is essential for cardiac trabeculation in vertebrate (*11*, *17*, *18*), showed high enrichment in CM-Vs but also exhibited notable intrinsic variations in expression levels (fig. S1C).

[1]Department of Cardiology, Center for Genetic Medicine, the Fourth Affiliated Hospital, Zhejiang University School of Medicine, Yiwu, Zhejiang, China. [2]International School of Medicine, International Institutes of Medicine, Zhejiang University, Yiwu 322000, China. [3]Institute of Genetics, Zhejiang University School of Medicine, Hangzhou, Zhejiang, China. [4]Institute of Molecular Medicine, National Biomedical Imaging Center, College of Future Technology, Peking-Tsinghua Center for Life Sciences, Peking University, Beijing 100871, China. [5]Women's Hospital, Zhejiang University School of Medicine, Hangzhou, Zhejiang, China. [6]Beijing Key Laboratory of Cardiometabolic Molecular Medicine, Institute of Molecular Medicine, College of Future Technology, and State Key Laboratory of Natural and Biomimetic Drugs, Peking University, Beijing 100871, China. [7]Institute of Neuroscience, State Key Laboratory of Neuroscience, CAS Center for Excellence in Brain Science and Intelligence Technology, Chinese Academy of Sciences, Shanghai 200031, China.
*Corresponding author. Email: hanpd@zju.edu.cn (P.H.); lijia@ion.ac.cn (J.L.)

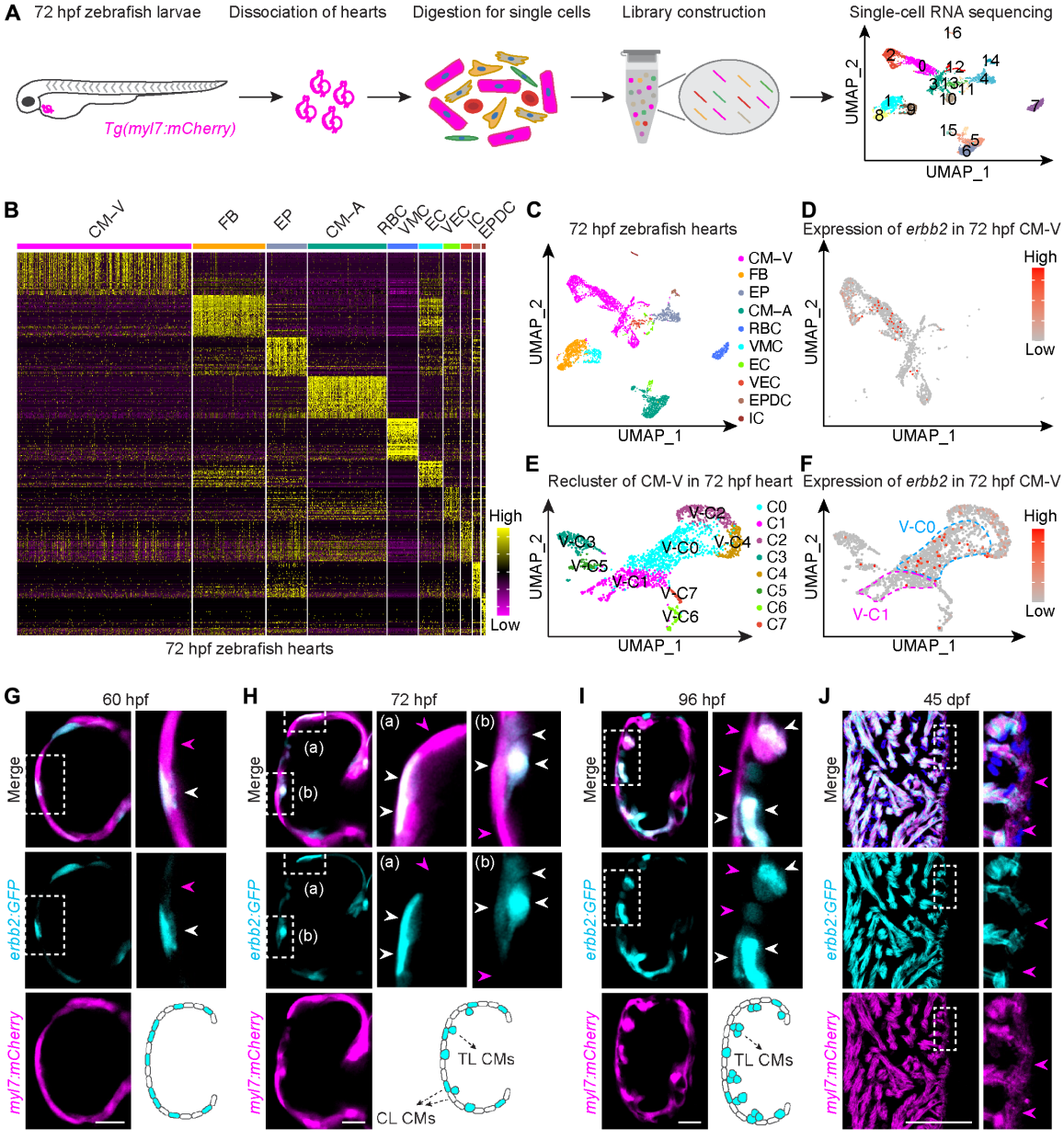

Fig. 1. Variations in *erbb2* expression in developing heart. (**A**) Schematic diagram illustrating the purification of embryonic hearts, isolation of cardiac cells, and subsequent single-cell RNA sequencing analysis. (**B**) Heatmap showing the expression of enriched markers in cell clusters of zebrafish hearts at 72 hours postfertilization (hpf). CM-V, ventricular cardiomyocytes; FB, fibroblasts; EP, epicardial cells; CM-A, atrial cardiomyocytes; RBC, erythrocytes; VMC, valve myocardial cell; EC, endocardial cells; VEC, valve endocardial cells; IC, immune cells; EPDC, epicardium-derived cells. Yellow, high expression; magenta, low expression. (**C**) UMAP plot showing the cardiac cell clusters in zebrafish hearts at 72 hpf. (**D**) UMAP plot showing the heterogeneous expression of *erbb2* in CM-V subpopulations. (**E**) UMAP plot showing reclustering of CM-V. (**F**) *erbb2* heterogeneity in CM-V. Red, high expression; gray, low expression. Three independent experiments were performed. (**G** to **I**) Confocal slices of cardiac ventricles expressing *erbb2:GFP;myl7:mCherry* at (G) 60 hpf, (H) 72 hpf, and (I) 96 hpf. (**J**) Confocal sections of *erbb2:GFP;myl7:mCherry* hearts at 45 days postfertilization (dpf). Enlarged views of boxed areas are shown in the right panels. White arrowheads, *erbb2:GFP*$^{+}$ cardiomyocytes; magenta arrowheads, *erbb2:GFP*$^{-}$ cardiomyocytes. CL CMs, compact layer cardiomyocytes; TL CMs, trabecular layer cardiomyocytes. [(G) to (J)] $n = 10$ zebrafish for each stage. Scale bars, 20 μm [(G) to (I)] and 100 μm (J).

By 72 hpf, epicardium-derived cells (EPDCs), valve myocardial cells (VMCs), and valve ECs (VECs) were detected, which were not present at 48 hpf (table S2 and Fig. 1, A to C). On the basis of the marker genes of cardiomyocytes, we identified clusters 0, 2, 3, 10, and 12 as CM-V and clusters 5, 6, and 15 as CM-A (table S2 and Fig. 1, A to C). We found that *erbb2* expression is heterogeneous in the developing ventricle, being highly enriched in subclusters 0 and 2, yet weakly expressed in subclusters 3, 10, and 12 (Fig. 1, A to D). Further reclustering of CM-V identified eight subclusters, including trabecular cardiomyocytes (V-C0) and compact layer cardiomyocytes (V-C1) (Fig. 1E), with *erbb2* expression highly enriched in the trabecular cardiomyocyte cluster (Fig. 1F).

To directly visualize the spatiotemporal expression of *erbb2* in developing embryos, we generated an *erbb2:Gal4* knock-in zebrafish (fig. S2A), which was subsequently crossed with *UAS:GFP* to obtain an *erbb2:Gal4;UAS:GFP* line, abbreviated as *erbb2:GFP*. Confocal imaging of *erbb2:GFP* zebrafish from 48 to 96 hpf revealed prominent expression of *erbb2* in the heart and skeletal muscles (fig. S2B). To enhance the spatial resolution of *erbb2* localization within the heart, we crossed *erbb2:GFP* with *myl7:mCherry* and *kdrl:mCherry* lines, which label cardiomyocytes and endothelial cells, respectively. At 96 hpf, the GFP signal was present exclusively in *myl7:mCherry*$^+$ cardiomyocytes (fig. S2C), with minimal colocalization between *erbb2:GFP* and *kdrl:mCherry* (fig. S2D). This observation is consistent with the well-documented role of *erbb2* in regulating cardiomyocyte function without impacting endocardium development (*18*). Furthermore, RNAscope analysis revealed that *erbb2* mRNA colocalized with *erbb2:GFP* in the developing heart (fig. S2E), corroborating the fidelity of this knock-in line.

We next explored the dynamic expression patterns of *erbb2* in the myocardium across different developmental stages. At 36, 48, and 60 hpf, cardiomyocytes in the single-layered myocardium could be distinguished based on their *erbb2* expression levels, with some carrying high *erbb2* (*erbb2:GFP*$^+$, white arrowheads) and others showing low *erbb2* expression (*erbb2:GFP*$^-$, magenta arrowheads) (Fig. 1G and fig. S2, F and G). With the emergence of nascent trabeculae at 72 and 96 hpf, cardiomyocytes within these trabeculae exhibited strong *erbb2:GFP* fluorescence, while those in the compact layer displayed mosaic *erbb2:GFP* expression (Fig. 1, H and I). We further quantified the proportion of *erbb2:GFP*$^+$ cells in both the compact and trabecular layers using *myl7:H2A-mCherry*, which specifically labels cardiomyocyte nuclei. Compared to 72-hpf embryos, the percentage of *erbb2:GFP*$^+$ cardiomyocytes in the compact layer of 96-hpf hearts decreased from approximately 78 to 58%, while the proportion within the trabeculae increased from about 48 to 66% (fig. S2H). As the embryos developed to 7 days postfertilization (dpf), expression of *erbb2:GFP* became specifically confined to trabecular cardiomyocytes (fig. S2I). This distinct pattern persisted through the young adult stage (45 days; Fig. 1J) and continued into adulthood (fig. S2J). Overall, the heterogeneity of *erbb2* expression coincides with trabeculae formation in the developing heart.

The expression levels of *erbb2* are directly associated with trabecular formation

Subsequently, we used lineage tracing analysis to monitor the fate of *erbb2*$^+$ cells. To this end, photoactivatable green fluorescent protein (PAGFP) (*19*) mRNA was injected into one-cell stage *erbb2:RFP;*β*-act2:BSR* embryos. At 60 hpf, illuminating single cardiomyocytes with a 405-nm laser activated the PAGFP signal (Fig. 2, A and B). Notably, by 80 hpf, approximately 80% of the PAGFP$^+$RFP$^+$ cells had delaminated (magenta arrowheads), whereas the majority of PAGFP$^+$ RFP$^-$ cardiomyocytes remained within the compact layer (white arrowheads) (Fig. 2, A to C). In a different approach, we crossed the *erbb2:Gal4* with the photoconvertible *UAS:Kaede* (*20*) fish to obtain the *erbb2:Gal4;UAS:Kaede* line, abbreviated as *erbb2:Kaede*. Similarly, when *erbb2:Kaede*$^+$ cardiomyocytes were photoconverted at 60 hpf, these cells also underwent delamination and preferentially contributed to trabeculae by 80 hpf (fig. S3, A to D).

To track the dynamic delamination of cardiomyocytes in the beating zebrafish heart, we used light-sheet microscopy coupled with a heartbeat detection and synchronization module. This setup enabled image acquisition exclusively during the cardiac diastole phase (*21*) (Fig. 2D). By mapping the movement trajectories of cardiomyocytes in *erbb2:GFP;myl7:H2A-mCherry* hearts from 60 to 80 hpf, we observed that *erbb2:GFP*$^+$ cells migrated toward the ventricular lumen, thereby seeding the trabecular layer (Fig. 2, E and F; fig. S3E, blue arrowheads; and movie S1, blue arrowheads). In contrast, *erbb2:GFP*$^-$ cardiomyocytes exhibited stochastic movements within the compact layer (Fig. 2, E and F; fig. S3E, white arrowheads; and movie S1, magenta arrowheads). The apicobasal movement distances of *erbb2:GFP*$^+$ cells were significantly longer than those of *erbb2:GFP*$^-$ cells (Fig. 2, F to H). Therefore, these results indicate that *erbb2* expression correlates with the sprouting of cardiomyocytes.

Differential *erbb2* expression controls tension heterogeneity to direct cardiomyocyte delamination

Previous work demonstrated that tension heterogeneity induces the delamination of a subset of cardiomyocytes to form trabeculae (*15*). Therefore, we investigated whether the differential expression of *erbb2* coincides with actomyosin tension. Through the analysis of phosphorylated myosin light chain (p-myo) (Fig. 3A), a marker of actomyosin tension, along with F-actin staining and fluorescence intensity profiling (fig. S4A), we observed that these markers were enriched on the apical side of *erbb2:GFP*$^+$ cardiomyocytes. In sharp contrast, adjacent *erbb2:GFP*$^-$ cells displayed a more diffusive distribution of these markers (Fig. 3A and fig. S4A). An apical view from the maximum intensity projection of F-actin (Fig. 3B) revealed a dense and highly branched filamentous network on the apical side of *erbb2:RFP*$^+$ cardiomyocytes. In contrast, F-actin in *erbb2:RFP*$^-$ cells exhibited a more diffuse arrangement on the apical side, with concentrations noted along the lateral sides (Fig. 3B). Similarly, by generating a transgenic line containing the fluorescence protein-tagged wild-type myosin regulatory light chain (*myl7:WT-MYL9-mRuby*), we demonstrated that WT-MYL9-mRuby proteins were enriched in *erbb2:GFP*$^+$ cells compared to neighboring *erbb2:GFP*$^-$ cells (Fig. 3C). In addition, fluorescence recovery after photobleaching (FRAP) analysis unveiled a significant reduction in the mobile fraction of WT-MYL9-mRuby proteins in *erbb2:GFP*$^+$ cardiomyocytes, which suggests a stabilization of the actomyosin network and higher cellular tension in these cells (Fig. 3D). These findings collectively suggest that differential *erbb2* activity correlates with actomyosin tension heterogeneity.

We further interrogated the interplay between *erbb2* expression and tension heterogeneity by using pharmacological and genetic approaches. Following treatment with the *erbb2* inhibitors PD168393 and AG1478, the enriched tension markers on the apical domain of *erbb2:GFP*$^+$ cardiomyocytes were completely abolished, compared to the dimethyl sulfoxide (DMSO) control (Fig. 3E and fig. S4, B to D). Likewise, maximum intensity projection of confocal images revealed that F-actin levels diminished at the apical side but accumulated laterally upon *erbb2* inhibition (fig. S4E). As expected, inactivating *erbb2* activity blocked cardiomyocyte delamination and trabeculae formation (Fig. 3E and fig. S4, B to D). Although *erbb2* lacks the capacity to bind ligands, it can dimerize with other ligand-binding *erbb* receptors to regulate downstream signaling (*22*). Previous studies have generated a dominant-negative form of human ERBB2 (DN-ERBB2) (*23*, *24*) lacking the cytoplasmic domain (Fig. 3F). Accordingly, we suppressed *erbb2* activity in individual cardiomyocytes by injecting

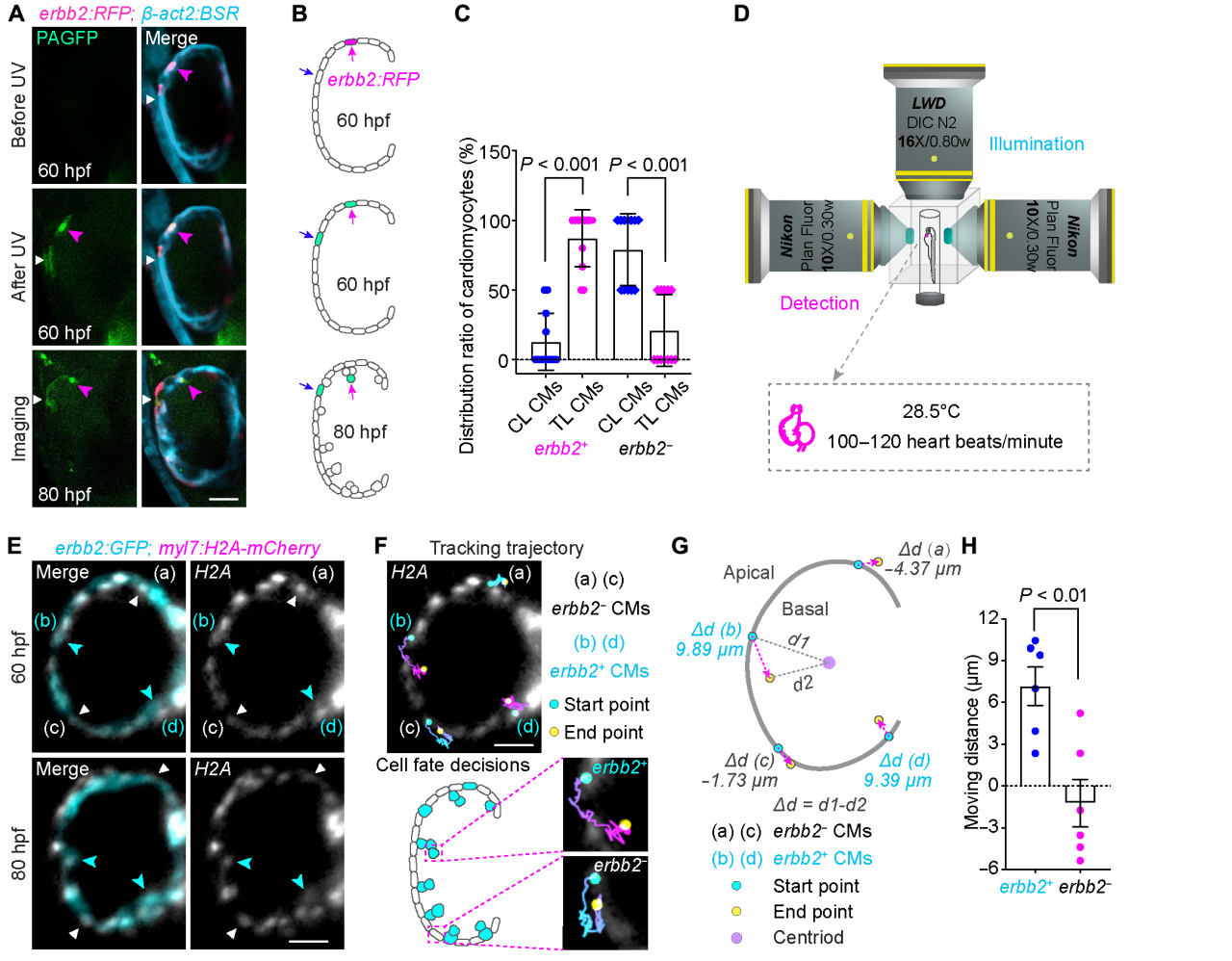

Fig. 2. The *erbb2* heterogeneity correlates with trabeculae formation. (**A**) *erbb2:RFP;β-act2:BSR* embryos were injected with photoactivatable green fluorescent protein (PAGFP) mRNA at the one-cell stage. Time series images of the same embryonic heart at 60 hpf before ultraviolet (UV) photoactivation (top), immediately following photoactivation (middle), and at 80 hpf (bottom). Magenta arrowheads: *erbb2:GFP*$^{+}$ cardiomyocytes; white arrowheads: *erbb2:GFP*$^{-}$ cardiomyocytes. (**B**) Schematic of photoactivation experiments to track the delamination of single cardiomyocytes in (A). (**C**) Quantification of the spatial distribution of *erbb2*$^{+}$ and *erbb2*$^{-}$ cardiomyocytes in the trabecular and compact layers at 80 hpf in (A). $n = 12$ embryos. (**D**) Schematic diagram showing the dual-side illumination objectives coupled with an imaging module. (**E**) Time-lapse images of *erbb2:GFP;myl7:H2A-mCherry* heart between 60 and 80 hpf. Blue and white arrowheads indicate *erbb2*$^{+}$ and *erbb2*$^{-}$ cardiomyocytes, respectively. (**F**) Curved lines in (E) represent the moving trajectories of *erbb2*$^{+}$ (magenta) and *erbb2*$^{-}$ (blue) cardiomyocyte nuclei. Blue circles indicate the starting points, and yellow circles denote the end points. (**G**) The schematic depicts the distance along the apicobasal axis of cell delamination over a 20-hour time window. (**H**) Quantification of the movement distance of *erbb2*$^{+}$ and *erbb2*$^{-}$ cardiomyocytes. $n = 12$ cardiomyocytes per group. For in toto live imaging, three independent experiments were performed using different hearts on different days. Data are presented as mean ± SEM. Two-tailed Mann-Whitney *U* tests were used for comparison. Scale bars, 25 μm.

(*myl7:DN-ERBB2-P2A-mCherry*) plasmid into embryos. The vast majority of *DN-ERBB2-P2A-mCherry*$^{+}$ clones remained within the compact layer at both 72 and 96 hpf (Fig. 3, G and H) and exhibited a reduction in cell tension (fig. S4F). Moreover, examination of *myl7:DN-ERBB2-P2A-mCherry* transgenic hearts revealed a decrease in F-actin at the apical side, accompanied by an accumulation on the lateral sides (Fig. 3I and fig. S4G). Therefore, *erbb2* appears to cell-autonomously promote actomyosin tension. Cardiomyocytes in *myl7:DN-ERBB2-P2A-mCherry* transgenic hearts exhibited a reduced apicobasal axis length compared to controls (fig. S4, H and I), while overall ventricular size was unaltered (fig. S4J), consistent with the previously reported phenotype in *erbb2* mutants (*6*, *18*).

Next, we explored whether enhancing cell tension could rescue the delamination defect observed in *erbb2*-deficient hearts. To this end, we generated a transgenic *myl7:CA-MYL9-mRuby* line carrying a constitutively active form of MYL9 (CA-MYL9) (*25*) (fig. S5A). Using a *BRE:d2GFP* transgenic line to label trabecular cardiomyocytes (*6*), live imaging demonstrated extensive trabeculae formation in hearts overexpressing CA-MYL9 compared to those expressing WT-MYL9 expression (fig. S5B). Notably, the hyper-trabeculation phenotype persisted in *myl7:CA-MYL9-mRuby* hearts, even after treatment with PD168393 and AG1478 (Fig. 3J and fig. S5C). Furthermore, clonal analysis using *myl7:DN-ERBB2-P2A-GFP* revealed that *DN-ERBB2-P2A-GFP*$^{+}$ cardiomyocytes in *myl7:CA-MYL9-mRuby* hearts tended to localize toward the trabecular layer (Fig. 3, K

and L, right). In contrast, *DN-ERBB2-P2A-GFP*$^+$ clones were predominantly found in the compact layer of *myl7:WT-MYL9-mRuby* hearts (Fig. 3, K and L, left). Together, these results demonstrate that *erbb2* promotes actomyosin tension in a cell-autonomous manner. It shows that increased tension can rescue the compromised delamination observed in *erbb2*-deficient cells.

On the other hand, we explored whether altering cardiomyocyte tension affected *erbb2* expression. In *erbb2:GFP* embryos injected with *myl7:WT-MYL9-mRuby*, *myl7:CA-MYL9-mRuby*, or a dominant-negative MYL9 (DN-MYL9) (*15*, *25*) (*myl7:DN-MYL9-mRuby*) plasmids, the GFP fluorescence intensity in *mRuby*$^+$*GFP*$^+$ cardiomyocytes was similar to that in *mRuby*$^-$*GFP*$^+$ cells within the same heart (fig. S5D). Similarly, when *erbb2:GFP* was crossed with the *myl7:WT-MYL9-mRuby*, *myl7:DN-MYL9-mRuby*, or *myl7:CA-MYL9-mRuby* transgenic lines, the overall GFP fluorescence intensity remained unchanged across all groups (fig. S5E). Thus, it appears that *erbb2* controls cell tension, while manipulation of cardiomyocyte tension has minimal impact on *erbb2* expression.

In addition, live imaging demonstrated that cardiomyocytes in *myl7:CA-MYL9-mRuby* transgenics exhibited a shorter apical domain and a longer apicobasal axis compared to *myl7:WT-MYL9-mRuby* hearts. In contrast, the apicobasal axis length was markedly reduced in *myl7:DN-MYL9-mRuby* hearts (fig. S5F). Z-stack imaging and maximum projection further revealed reduced ventricular size in *myl7:CA-MYL9-mRuby* hearts and increased size in *myl7:DN-MYL9-mRuby* hearts (fig. S5G). These differences in cell shape and organ morphology are consistent with the modifications in myofibrillar structure observed in these transgenic lines.

erbb2 stimulates cardiomyocyte tension independently of its regulatory function in cell proliferation

Previous studies have shown that the loss of Erbb2 prevents trabeculae formation in both murine and zebrafish hearts (*6*, *18*, *24*). A recent study proposed that *erbb2* triggers organ-wide proliferation, thereby inducing cellular crowding and tension heterogeneity (*15*). Hence, we speculated that the impaired trabeculation in *erbb2*-deficient hearts might stem from compromised cell tension, as described above, or from a defect in proliferation. To distinguish between these possibilities, we examined cardiomyocyte proliferation in *myl7:DN-ERBB2-P2A-mCherry* hearts using the *myl7:Venus-hGeminin* line, which labels cardiomyocytes in the S/G2/M phases of the cell cycle (*26*). Notably, quantification of *Venus-hGeminin*$^+$ cardiomyocytes revealed no difference between *myl7:DN-ERBB2-P2A-mCherry* and control hearts (fig. S6A). Therefore, unlike previous studies that reported decreased cardiomyocyte proliferation in *erbb2* mutants or after PD168393/AG1478 treatment, *DN-ERBB2* appears to be a hypomorphic construct that decouples proliferation from cell tension. We thus reasoned that the absence of trabeculae formation in *myl7:DN-ERBB2-P2A-mCherry* hearts resulted from defective cell tension rather than from impaired proliferation.

Furthermore, we injected a low concentration of the *myl7:DN-ERBB2-P2A-mCherry* plasmid into *myl7:Venus-hGeminin* to generate one to three clones per heart. As expected, these DN-ERBB2 clones were still able to proliferate but failed to delaminate (fig. S6B). Moreover, by treating embryos with the vitamin D analog alfacalcidol (alfa) to stimulate cardiomyocyte proliferation (*27*) and trabeculation (*15*), DN-ERBB2 clones still remained in the compact layer, although prominent trabeculation was observed in their neighboring cells (fig. S6C). Notably, these results are in agreement with previous blastomere transplantation studies, where transplanted single *erbb2*$^{-/-}$ clones consistently stayed within the compact layer and were less likely to influence the proliferation of neighboring cells (*6*, *15*, *18*), supporting the role of *erbb2* in directly regulating cell tension. Collectively, our findings indicate that *erbb2* promotes cardiomyocyte tension to direct their sprouting, independently of its function in regulating proliferation.

erbb2 promotes trabeculation through inducing PI3K activity

Next, we aim to unravel the molecular machinery by which *erbb2* controls actomyosin tension. *erbb2* belongs to the receptor tyrosine kinase (RTK) family, which primarily transmits downstream signaling through the phosphatidylinositol 3-kinase (PI3K)–Akt axis (*28*, *29*). Activated PI3K generates phosphatidylinositol-3,4-bisphosphate [PtdIns(3,4)P_2] and phosphatidylinositol-3,4,5-trisphosphate [PtdIns(3,4,5)P_3], which bind to the pleckstrin homology (PH) domain of AKT (*30*, *31*). Thus, the activity of PI3K can be visualized by the recruitment of the PH-AKT-GFP probe to the membrane (*31*, *32*). To this end, we created a *myl7:PH-AKT-GFP* zebrafish line and crossed it with *erbb2:RFP* to simultaneously visualize *erbb2* expression and PI3K activity. Confocal imaging and fluorescence intensity profiling revealed an enrichment of PH-AKT-GFP at the plasma membrane in *erbb2:RFP*$^+$ cardiomyocytes at 60 and 72 hpf (Fig. 4A and fig. S7A), indicating PI3K activation. In sharp contrast, a cytosolic distribution of PH-AKT-GFP was evident in *erbb2:RFP*$^-$ cells within the same heart (Fig. 4A and fig. S7A). These differences in PH-AKT-GFP localization were further elucidated through maximum intensity projections (fig. S7B). After treatment with PD168393 and AG1478, plasma membrane localization of PH-AKT-GFP in *erbb2:RFP*$^+$ cells was completely abolished (Fig. 4B and fig. S7, C to E). Similarly, a cytosolic localization of PH-AKT-GFP was detected in transgenic *myl7:DN-ERBB2-P2A-mCherry* hearts (Fig. 4C and fig. S7F). Moreover, treating embryos with the PI3K inhibitor LY294002 largely eliminated the membrane enrichment of PH-AKT-GFP in *erbb2:RFP*$^+$ cells (Fig. 4D), confirming the fidelity of this probe in monitoring PI3K activity. In eukaryotic cells, PI3K plays a pivotal role in actin polymerization to generate mechanical force and drive cell migration (*33*). Inhibiting PI3K with LY294002 led to reduced F-actin in the apical domain of cardiomyocytes and concurrently excessive myofibrils at the lateral sides (fig. S7, G and H), mirroring observation in *erbb2*-deficient hearts. Overall, these results indicate that *erbb2* promotes PI3K activity in cardiomyocytes.

The PI3K-Arp2/3 axis directly initiates remodeling of the actomyosin network

Given that the actin-related protein-2/3 (Arp2/3) complex is a key PI3K signaling mediator that modulates actin filament nucleation (*34*), we analyzed its components through immunostaining and detected membrane-enriched Arp2 and Arp3 in the myocardium (fig. S8, A and B). Moreover, upon injecting a *myl7:actr2b-mRuby* plasmid encoding the zebrafish Arp2b protein (actr2b) into *myl7:memGFP* embryos, we observed an enrichment of the actr2b-mRuby protein on the plasma membrane of delaminating cardiomyocytes (Fig. 4E). However, following exposure to PD168393, AG1478, or LY294002, the membrane localization of Arp2/3 and actr2b-mRuby was largely abolished (Fig. 4E and fig. S8, A and B). To directly visualize whether PI3K activity in *erbb2*$^+$ cells triggered Arp2/3 accumulation, we generated a transgenic *myl7:actr2b-mRuby* line. Confocal images

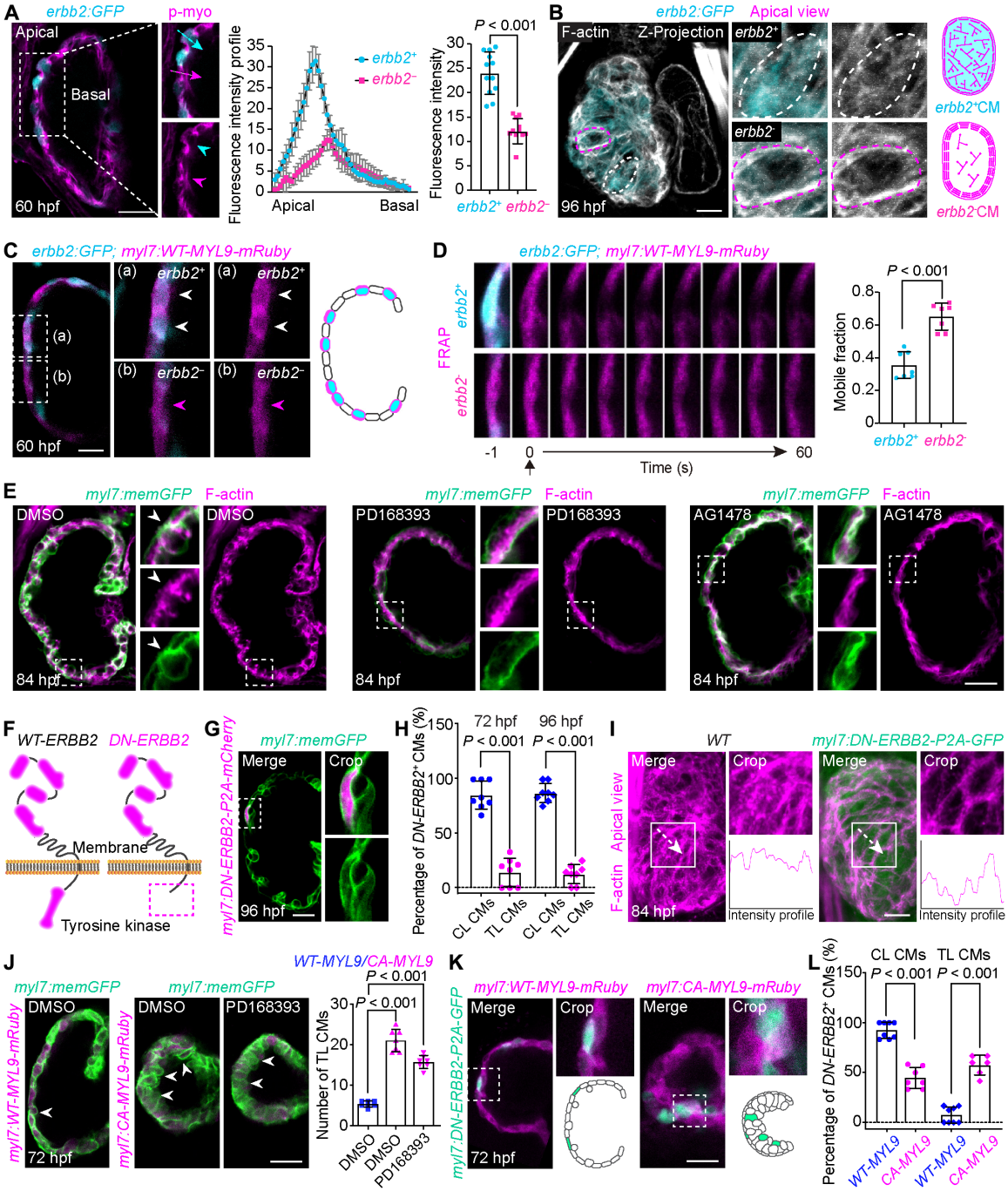

Fig. 3. *erbb2* directly controls tension heterogeneity to guide cardiomyocyte delamination. (**A**) Left, p-myo staining in *erbb2:GFP* hearts at 60 hpf. Dashed arrows, the positions subjected to fluorescence intensity profiling; blue and magenta arrowhead, *erbb2:GFP*$^{+}$ and *erbb2:GFP*$^{-}$ cardiomyocytes, respectively. Middle and right: fluorescence intensity profiles and average fluorescence intensities of p-myo. $n = 12$ cardiomyocytes for each group. (**B**) Apical view and schematics of F-actin maximum intensity projections in *erbb2:GFP* embryos at 96 hpf. White and magenta dashed lines, *erbb2*$^{+}$ and *erbb2*$^{-}$ cells, respectively. (**C**) Confocal image of *erbb2:GFP;myl7:WT-MYL9-mRuby* embryo at 60 hpf. White and magenta arrowheads, *erbb2:GFP*$^{+}$ and *erbb2:GFP*$^{-}$ cardiomyocytes. (B and C) $n = 7$ embryos. (**D**) Fluorescence recovery after photobleaching (FRAP) analysis of WT-MYL9-mRuby in *erbb2:GFP;myl7:WT-MYL9-mRuby* hearts. Right: quantifications of WT-MYL9-mRuby mobile fraction. $n = 7$ cardiomyocytes for each group. (**E**) F-actin staining in *myl7:memGFP* hearts treated with DMSO, PD168393, and AG1478. Arrowheads, the apical enrichment of F-actin. (**F**) Schematic of a dominant-negative human *ERBB2* (*DN-ERBB2*). (**G**) *myl7:DN-ERBB2-P2A-mCherry* clones were confined to the compact layer at 96 hpf. (**H**) Quantifications of the spatial distributions of DN-ERBB2 clones at 72 and 96 hpf. CL CMs, compact layer cardiomyocytes; TL CMs, trabecular layer cardiomyocytes. [(E), (G), and (H)] $n = 8$ embryos for each stage. (**I**) Apical view and schematics of F-actin in *WT* and *myl7:DN-ERBB2-P2A-GFP* hearts. (**J**) Confocal image and statistics of trabeculae in *myl7:WT-MYL9-mRuby* (left), *myl7:CA-MYL9-mRuby* treated with DMSO (middle), and PD168393 (right) at 72 hpf. Arrowheads, trabeculae. (**K**) Confocal image showing DN-ERBB2-P2A-GFP^{+} clones in *myl7:WT-MYL9-mRuby* and *myl7:CA-MYL9-mRuby* hearts. (**L**) Quantifications of DN-ERBB2 clone distributions in (**K**). [(I) to (L)] $n = 7$ to 10 embryos for each group. Data are presented as mean ± SEM. Unpaired two-tailed Student's *t* tests [(A) and (D)], one-way ANOVA (J), and two-tailed Mann-Whitney U tests [(H) and (L)] were applied to assess statistical significance. Scale bars, 20 μm.

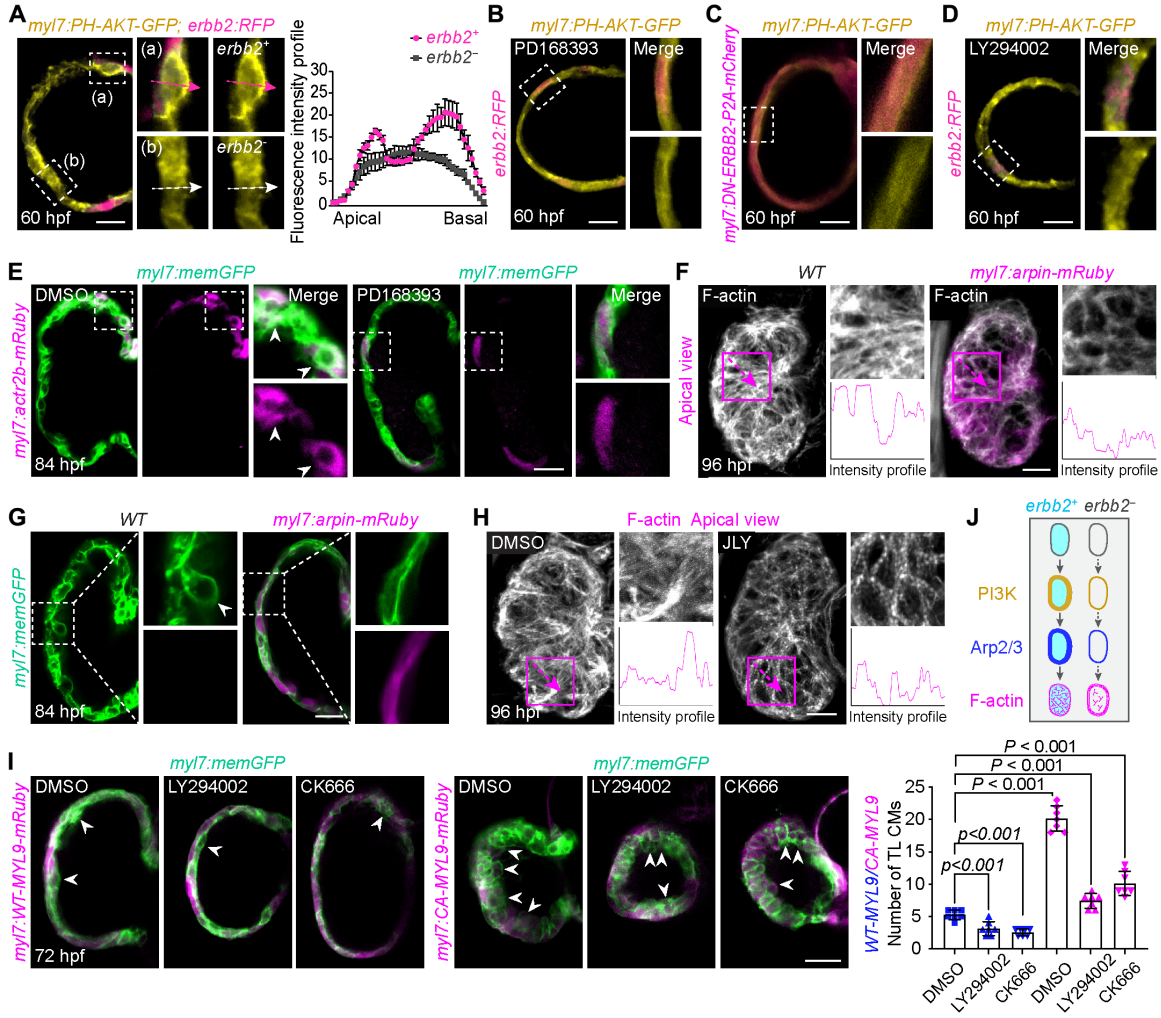

Fig. 4. *erbb2* promotes trabeculation by triggering PI3K-mediated remodeling of the actomyosin network. (**A**) Confocal imaging of *myl7:PH-AKT-GFP;erbb2:RFP* hearts at 60 hpf. PH-AKT-GFP was enriched on the plasma membrane of *erbb2:RFP*$^{+}$ cardiomyocytes, while its cytosolic distribution was observed in *erbb2:RFP*$^{−}$ cells. Insets are magnifications of boxed areas, and the dashed arrows indicate the position subjected to fluorescence intensity analysis. Right: fluorescence intensity profiles of PH-AKT-GFP. $n = 10$ embryos. (**B**) PD168393-treated *myl7:PH-AKT-GFP;erbb2:RFP* heart at 60 hpf. (**C**) Confocal image of *myl7:PH-AKT-GFP;myl7:DN-ERBB2-P2A-mCherry* heart at 60 hpf. (**D**) *myl7:PH-AKT-GFP;erbb2:RFP* hearts treated with LY294002 to inhibit PI3K signaling. [(B) to (D)] $n = 8$ embryos. (**E**) *myl7:memGFP* embryos, carrying *myl7:actr2b-mRuby* clones, were treated with DMSO (left) and PD168393 (right). Arrowheads denote the membrane localization of the actr2b-mRuby in delaminating cardiomyocytes. (**F**) Apical views of maximum intensity projections of F-actin in wild-type (WT) and *myl7:arpin-mRuby* hearts. F-actin is restricted to the lateral sides of cardiomyocytes in *myl7:arpin-mRuby* hearts. (**G**) Confocal images of *myl7:memGFP* (left) and *myl7:arpin-mRuby;myl7:memGFP* (right) hearts at 84 hpf. Arrowheads, trabeculae. (**H**) Apical views of F-actin network in DMSO and JLY-treated hearts. JLY decouples PI3K signaling from its ability to regulate actin dynamics. JLY, a combination of jasplakinolide (0.8 μM), latrunculin A (0.125 μM), and Y27632 (1 μM). [(E) to (H)] $n = 6$ to 10 embryos per group. Insets are enlarged views of boxed areas. [(F) and (H)] Dashed arrows indicate the intensity profile of F-actin. (**I**) Confocal images of 72 hpf *myl7:WT-MYL9-mRuby;myl7:memGFP* (left) and *myl7:CA-MYL9-mRuby;myl7:memGFP* (right) embryos treated with DMSO, LY294002, and CK666. Arrowheads indicate trabeculae. Quantifications of trabeculae are displayed on the right. $n = 7$ embryos per group. One-way ANOVA, followed by Tukey's multiple comparisons test was used. Data are presented as mean ± SEM. Scale bars, 20 μm. (**J**) Schematic diagram showing *erbb2* promotes actomyosin network remodeling through the PI3K-Arp2/3 axis.

showed that only cardiomyocytes carrying *erbb2* and PI3K activities exhibited membrane-localized Actr2b, in sharp contrast to *erbb2* and PI3K-deficient cells (fig. S8, C and D). Furthermore, inhibiting *erbb2* disrupted the membrane accumulation of actr2b-mRuby (fig. S8E).

Subsequently, to explore the effects of perturbing Arp2/3 activity, we used both pharmacological and genetic approaches. Treatment with the Arp2/3 inhibitor CK666 completely eliminated the apical enrichment of F-actin (fig. S9, A and B), a result that mirrors observations in *erbb2* and PI3K-inhibited hearts. Furthermore, we constructed a *myl7:arpin-mRuby* transgenic line that expresses Arpin, an endogenous inhibitor of the Arp2/3 complex (*35*). Confocal imaging demonstrated that F-actin accumulated at the lateral sides of cardiomyocytes in *myl7:arpin-mRuby* hearts (Fig. 4F), which was accompanied by conspicuous delamination defects and confinement of these cells to the compact layer (Fig. 4G). Notably, cardiomyocytes in *myl7:arpin-mRuby* transgenic hearts exhibited a decreased apicobasal axis length (fig. S9C), while overall ventricular size was

unchanged compared to controls (fig. S9D). On the other hand, clonal analysis revealed that the presence of Arpin did not affect *erbb2* intensity (fig. S9E) or the membrane accumulation of PH-AKT-GFP (fig. S9F), suggesting that Arp2/3 functions downstream of the *erbb2*-PI3K axis to regulate cell tension.

To decouple PI3K signaling from its ability to regulate actin dynamics, we used a combination of jasplakinolide (an inducer of actin polymerization), latrunculin A (an inhibitor of actin polymerization), and Y27632 (a Rho kinase inhibitor), collectively referred to as the JLY cocktail. This approach blocks actin dynamics while preserving the existing F-actin organization (*31*). In JLY-treated embryos, *erbb2:RFP*$^+$ cells continued to exhibit a pronounced PH-AKT-GFP signal at the plasma membrane (fig. S9G) but were unable to establish apical F-actin (Fig. 4H). Furthermore, trabeculae formation was also disrupted following JLY treatment (fig. S9G, arrowheads). These observations suggest that the dynamics of apical F-actin, rather than the cytoskeleton structure itself, are required for cardiomyocyte delamination.

We further investigated the cross-talk between PI3K-Arp2/3 and cell tension. As expected, exposure to LY294002 and CK666 led to a significant disturbance in trabeculation in *myl7:WT-MYL9-mRuby* hearts at 60 and 72 hpf (Fig. 4I and fig. S9H, left panels). In sharp contrast, *myl7:CA-MYL9-mRuby* embryos exhibited persistent trabeculae formation despite deficiencies in PI3K and Arp2/3 (Fig. 4I and fig. S9H, right panels), supporting the notion that enhanced cardiomyocyte tension can rescue delamination defects in hearts lacking functional PI3K and Arp2/3 activity. In summary, these results underscore the essential role of differentially expressed *erbb2* in promoting tension heterogeneity through the PI3K-Arp2/3 axis, ultimately controlling the onset of trabeculation (Fig. 4J).

Given that mechanical forces and cardiac contractility also affect trabeculation (*9*, *36*), we performed live imaging to assess the contractile function of the heart in transgenic lines that modulate either *erbb2* signaling or actomyosin tension. At 48 and 72 hpf, critical time points for trabeculae initiation, the contractility in *myl7:DN-ERBB2-P2A-mCherry*, *myl7:DN-MYL9-mRuby*, and *myl7:arpin-mRuby* hearts was comparable to that observed in control embryos (fig. S10, A to F). Hence, contractile forces are unlikely to play an essential role in regulating the *erbb2*-actomyosin axis to drive the onset of trabeculation. Notably, we observed a reduction in contractility in *myl7:CA-MYL9-mRuby* at 72 hpf (fig. S10, C and D), likely due to the smaller ventricular size and disrupted cardiomyocyte organization.

Notch-mediated lateral inhibition reinforces the trabecular pattern by suppressing *erbb2*

After the initiation of trabeculation, nascent trabeculae activate Notch signaling in adjacent cardiomyocytes to suppress their delamination through lateral inhibition machinery (*6*). To explore how Notch interplays with *erbb2* and cell tension, we collected hearts from embryos treated with either DMSO (control) or the Notch inhibitor DAPT (a chemical inhibitor of γ-secretase), and subsequently performed bulk RNA-sequencing (fig. S11A). Comparative analysis identified 4788 up-regulated and 5098 down-regulated genes in DAPT-treated hearts compared to the control group (fig. S11B). Notably, *erbb2* expression was significantly up-regulated following Notch inhibition (Fig. 5A), a finding that was further validated by quantitative real-time polymerase chain reaction (qRT-PCR) analysis (fig. S11C). Gene set enrichment analysis (GSEA) revealed an up-regulation of reactome PI3K events in Erbb2 signaling in DAPT-treated hearts (fig. S11D). In addition, the expression levels of key genes in PI3K-AKT signaling and actomyosin structure organization were enhanced (Fig. 5B and fig. S11E). GO enrichment analysis revealed that the up-regulated genes were primarily associated with processes such as muscle structure development, muscle cell differentiation, heart morphogenesis, and actomyosin structure organization (fig. S11F). Collectively, these results suggest that inhibiting Notch signaling promotes the *erbb2*-PI3K axis and enhances actomyosin tension.

We further performed live imaging to simultaneously visualize the spatiotemporal dynamics of *erbb2* and Notch activities. As previously described (*6*), *Tp1:d2GFP*$^+$ (Notch reporter) cardiomyocytes exhibited an intermittent distribution across the compact layer. *erbb2:RFP* fluorescence was absent in these *Tp1:d2GFP*$^+$ cells at 72 and 96 hpf (Fig. 5C and fig. S12A, top). Maximum intensity projections further highlighted the mutually exclusive allocations of *Tp1:d2GFP*$^+$ and *erbb2:RFP*$^+$ cardiomyocytes (Fig. 5C and fig. S12A, bottom). As expected, treating *erbb2:RFP;Tp1:d2GFP* embryos with DAPT resulted in a reduction in the *Tp1:d2GFP* signal (Fig. 5D and fig. S12B). Conversely, an increase in *erbb2:RFP*$^+$ fluorescence was observed upon Notch inhibition (Fig. 5D and fig. S12, B to E). In a complementary assay, activation of Notch signaling in cardiomyocytes was achieved by injecting a *myl7:NICD-P2A-GFP* plasmid into *erbb2:RFP* embryos. Intriguingly, the majority of *NICD-P2A-GFP*$^+$ clones were devoid of *erbb2:RFP* signal and remained confined to the compact layer (Fig. 5E). Since both Notch inhibition and activation in the myocardium do not affect the number of cardiomyocytes (*6*), we conclude that myocardial Notch signaling appears to suppress *erbb2* expression to restrict cell delamination.

We further interrogated the effects of Notch inhibition on PI3K activity and cell tension. *myl7:PH-AKT-GFP* embryos treated with DAPT exhibited a thickened ventricular layer and pronounced enrichment of PH-AKT-GFP at cell membranes (Fig. 5F), corroborating the increase in *erbb2* expression following Notch inhibition. Similarly, suppressing Notch activity resulted in a marked increase in apical F-actin (Fig. 5G). Hence, cell tension appears to function downstream of the Notch-*erbb2* axis. This is substantiated by the fact that DAPT treatment in *myl7:DN-MYL9-mRuby* failed to induce trabeculae formation (Fig. 5H), whereas enhancing cell tension in *myl7:CA-MYL9-mRuby* effectively rescued the delamination defect in *myl7:NICD-P2A-GFP* transgenic hearts (Fig. 5I). Together, these results indicate that Notch-mediated lateral inhibition abolishes *erbb2* expression, thereby sequestering cardiomyocytes in the compact layer. Conversely, suppression of Notch activity unleashes its inhibitory effect on *erbb2*, which in turn promotes cell tension and delamination.

DISCUSSION

In the present study, we generated multiple zebrafish lines to visualize the spatiotemporal dynamics of *erbb2* during the initiation and progression of cardiac trabeculation. Notably, the differential expression of *erbb2* coincides with variations in PI3K activity and tension heterogeneity. Cardiomyocytes expressing high levels of *erbb2* tend to undergo delamination and form nascent trabeculae, whereas those with low levels of *erbb2* remain in the compact layer. However, the regulatory mechanisms governing the divergent expression of *erbb2* remain unclear. Previous studies have suggested that zebrafish

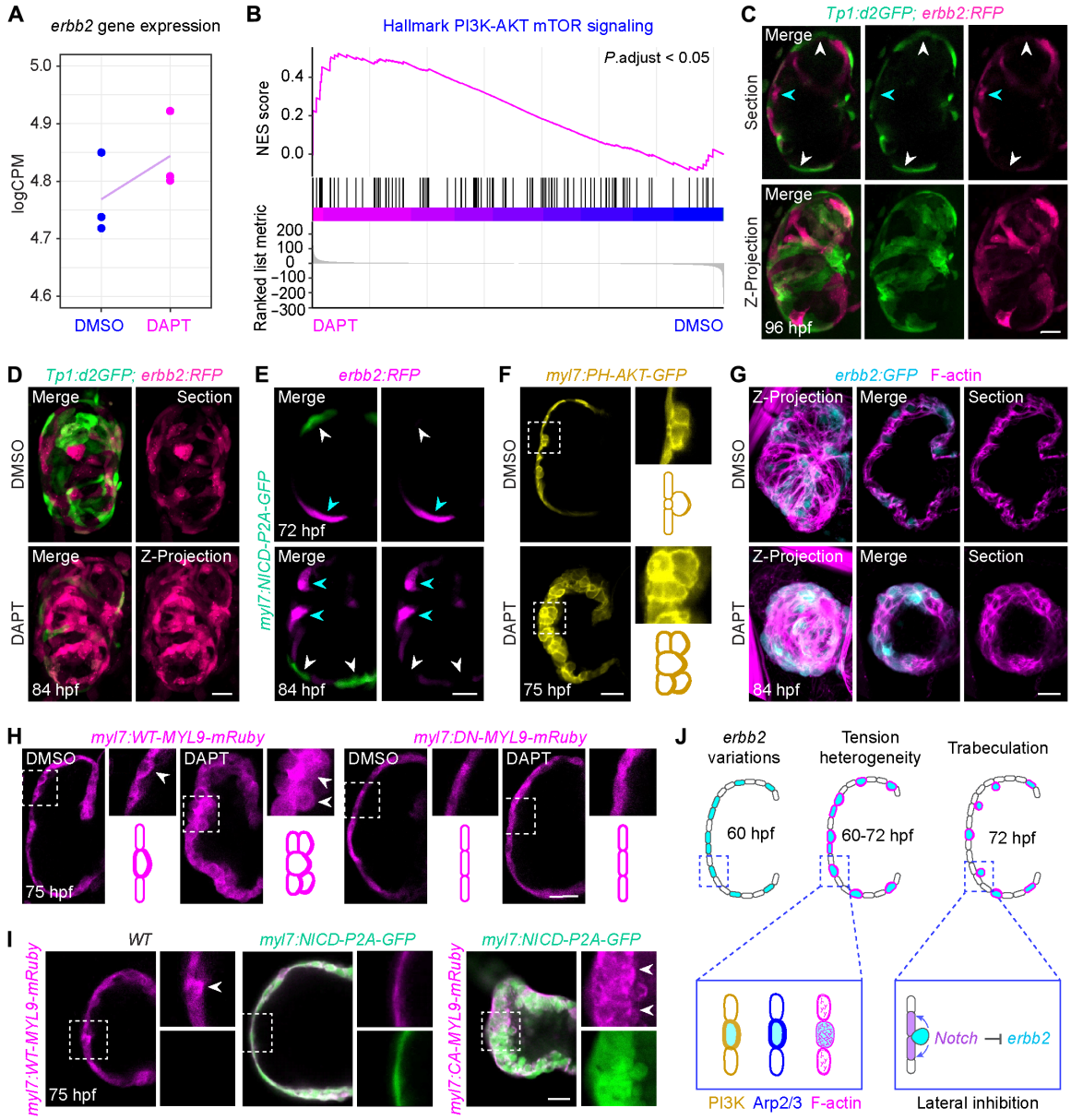

Fig. 5. Notch-mediated lateral inhibition suppresses trabeculation by reducing *erbb2* expression. *myl7:mCherry* embryos were treated with 100 μM DAPT and DMSO from 84 to 96 hpf. Three independent replicates were performed, with each replicate containing approximately 1000 embryonic hearts. (**A**) RNA sequencing analysis revealed that *erbb2* expression was significantly up-regulated following DAPT-treatment. (**B**) Gene set enrichment analysis (GSEA) revealed an increased expression level of key genes in the PI3K-AKT signaling pathway in Notch-inhibited hearts. Magenta, high expression; blue, low expression. (**C**) Confocal section (top) and maximum projections (bottom) of *Tp1:d2GFP;erbb2:RFP* heart at 96 hpf. Note the mutually exclusive distributions of *Tp1:d2GFP*$^+$ and *erbb2:RFP*$^+$ cells. White arrowheads, *Tp1:d2GFP*$^+$ cells; blue arrowheads, *erbb2:RFP*$^+$ cells. (**D**) Maximum projections of *Tp1:d2GFP;erbb2:RFP* embryos treated with DMSO and DAPT. (**E**) *erbb2:RFP* embryos were injected with the *myl7:NICD-P2A-GFP* plasmid at the one-cell stage and imaged at 72 and 84 hpf. White arrowheads, *NICD-P2A-GFP*$^+$ cells; blue arrowheads, *erbb2:GFP*$^+$ cells. (**F**) Confocal images of *myl7:PH-AKT-GFP* hearts exposed to DMSO and DAPT. Insets are magnifications of boxed areas. (C to F) $n = 10$ embryos per group. (**G**) F-actin staining of *erbb2:GFP* hearts after treatment with either DMSO or DAPT. (**H**) Confocal images of *myl7:WT-MYL9-mRuby* (left) and *myl7:DN-MYL9-mRuby* (right) embryos treated with DMSO and DAPT. Notably, inhibiting Notch activity was unable to rescue the trabeculation defects in *myl7:DN-MYL9-mRuby* hearts. (**I**) Confocal images of *myl7:WT-MYL9-mRuby* (left), *myl7:WT-MYL9-mRuby;myl7:NICD-P2A-GFP* (middle), and *myl7:CA-MYL9-mRuby;myl7:NICD-P2A-GFP* (right) hearts. [(G) to (I)] $n = 8$ embryos per group. Scale bar, 20 μm. (**J**) Schematic illustration of the trabeculae formation paradigm: Initially, *erbb2* is differentially expressed in the single-layer myocardium (left). Subsequently, *erbb2* activates the PI3K-Arp2/3 axis, inducing cell tension heterogeneity and cardiomyocyte sprouting (middle). Last, the nascent trabeculae trigger Notch activity in adjacent cardiomyocytes, which then abolishes their *erbb2* expression to confine these cardiomyocytes in the compact layer.

CM-Vs are derived from various developmental origins (*37*, *38*), raising the possibility that *erbb2*-high and *erbb2*-low cells are linked to these distinct progenitors. Alternatively, the expression of *erbb2* may be controlled by other upstream genetic or epigenetic factors, warranting further exploration.

As a canonical member of the RTK family, *erbb2* plays a crucial role in regulating various cellular events, including cell proliferation and delamination. However, its direct influence on actomyosin reorganization in cardiomyocytes remains controversial. Previous work using an actin-binding GFP reporter suggests a direct link between *erbb2* activity and the apical filamentous myofibrils network (*24*). Conversely, another study discounts the involvement of *erbb2* in regulating actomyosin (*15*). These discrepancies may arise from technical challenges associated with decoupling *erbb2*'s role in controlling proliferation from its impact on cell tension through genetic loss-of-function analysis. By using a dominant-negative form of *erbb2*, our results delineated these diverse functions. We propose that *erbb2* plays distinct roles during different phases of heart morphogenesis. In the heart tube stage, *erbb2* is crucial for cardiomyocyte proliferation, ensuring an adequate cell pool to support heart development. However, proliferation alone is insufficient to direct cardiomyocytes toward their delamination fate. Upon the initiation of trabeculation, the differentially expressed *erbb2* cell-autonomously activates the PI3K-Arp2/3 axis, which facilitates apical F-actin accumulation and drives cell delamination. This conclusion is supported by several lines of evidence: (i) DN-ERBB2 suppressed cardiomyocyte delamination without impacting their proliferation; (ii) stimulating cell proliferation to increase cellular crowding failed to promote the delamination of single DN-ERBB2 clones; and (iii) Notch activation suppressed *erbb2* expression and prevented cardiomyocyte delamination, while Notch inhibition expanded the expression of *erbb2* and facilitated trabeculation. Neither manipulation affects cardiomyocyte proliferation.

The present study has certain limitations. For instance, RNAscope analysis revealed that *erbb2* mRNA largely colocalized with *erbb2:GFP* in the myocardium of the developing heart, although some nonspecific RNAscope fluorescence was observed in blood cells within the ventricle. Notably, the *erbb2* mRNA signal did not fully overlap with *erbb2:GFP* in the myocardium. This may reflects differences in the stability of *erbb2* mRNA and GFP, or suggest that *erbb2:GFP* does not entirely recapitulate the endogenous expression pattern of *erbb2*. In addition, while our data, based on cardiac contractility measurement in the *myl7:DN-ERBB2-P2A-mCherry*, *myl7:DN-MYL9-mRuby*, and *myl7:arpin-mRuby* lines, suggest that mechanical forces are unlikely to play a critical role in regulating the *erbb2*-actomyosin axis during the initiation of trabeculation, we cannot exclude the possibility that the heartbeat may influence heart development at later stages. This possibility warrants further investigation.

In summary, these analyses establish a paradigm for ventricular wall formation. The heterogeneous expression of *erbb2* disrupts the symmetry of the single-layer myocardium, initiating the sprouting of cardiomyocytes through the PI3K-Arp2/3-cell tension axis. Subsequently, the nascent trabeculae trigger Notch activity in adjacent cardiomyocytes. This morphogenetic pattern is, therefore, reinforced by Notch-mediated lateral inhibition, achieved through the suppression of *erbb2* and cell tension (Fig. 5J). Together, these findings provide a comprehensive understanding of the genetic-mechanic cross-talk machinery that regulates ventricular wall morphogenesis.

MATERIALS AND METHODS

Zebrafish husbandry and strains

Zebrafish (*Danio rerio*) were maintained under standard laboratory conditions at 28°C. All zebrafish handling and experimental procedures were approved by the Institutional Animal Care and Use Committee of Zhejiang University (application no. 29296). The *erbb2:Gal4* knockin line was generated using a method previously described (*39*). Specifically, the zebrafish codon-optimized Cas9 (zCas9) expression plasmid, pGH-T7-zCas9 (*40*), was linearized by Xba I and used as a template for in vitro synthesis of Cas9 mRNA. Purification of mRNA was performed using the mMACHINE T7 Ultra kit (Ambion). The short guide RNA (sgRNA) sequence was designed for specific target selection to minimize off-target effects according to established criteria (*41*) (http://crispor.tefor.net/crispor.py). A sgRNA (TATAGTTGATACCAATAAAG) targeting the last exon of *erbb2* was used for generating the knockin line. In brief, a pair of oligonucleotides containing the sgRNA targeting sequence were annealed and cloned downstream of the T7 promoter in the PT7-sgRNA vector. The sgRNA was synthesized using the MAXIscript T7 Kit (Ambion) and purified with the mirVana miRNA Isolation Kit (Ambion).

The *erbb2-P2A-Gal4* donor plasmid was constructed by ligating the *erbb2* left arm [1471 base pairs (bp)], *erbb2* right arm (690 bp), and the DNA fragment of P2A-Gal4 into PMD-19-T using the In-Fusion Cloning Kit (Takara). The left and right arms for *erbb2* were amplified from wild-type zebrafish genomic DNA using the Q5 High-Fidelity DNA polymerase (New England Biolabs) with the following primers: Left arm amplification primers: F, 5′-AACCCTATAACAAATTCGCC-3′; and R, 5′- GGTGTACTCCTTGTGGCCGC-3′. Right arm amplification primers: F, 5′-TAAAGCTTTAGTGTGGGTGT-3′; and R, 5′-GAGGCTGGTGGTATTCTCCG-3′.

Subsequently, zCas9 mRNA, *erbb2* targeting sgRNA, and *erbb2* donor plasmid were co-injected into one-cell stage fertilized zebrafish embryos. Each embryo received 1 nl of solution containing zCas9 mRNA (750 ng/μl), sgRNA (100 ng/μl), and donor plasmid (25 ng/μl). To screen for *erbb2:Gal4* knockin founders, injected fish reaching adulthood were crossed with AB wild-type zebrafish. Genomic DNA was extracted from embryos at 72 hpf, and germline transmission was assessed by PCR and sequencing. Primers for genotyping the knockin fish at the 5′ junction were: *erbb2*-F1, 5′-GTGTGAAACGTAGCTCAGCG-3′; and *Gal4*-R1, 5′-AGTCAGCGGAGACCTTTTGG-3′. The *erbb2:Gal4* founders were then crossed with UAS lines to obtain *erbb2:Gal4;UAS:GFP* and *erbb2:Gal4;UAS:RFP*.

The following transgenic lines were generated through the Tol2 transposon system in this study: *Tg(myl7:DN-ERBB2-P2A-GFP)*, *Tg(myl7:DN-ERBB2-P2A-mCherry)*, *Tg(myl7:WT-MYL9-mRuby)*, *Tg(myl7:CA-MYL9-mRuby)*, *Tg(myl7:DN-MYL9-mRuby)*, *Tg(myl7:PH-AKT-GFP)*, *Tg(myl7:arpin-mRuby)*, *Tg(myl7:actr2b-mRuby)*, and *Tg(myl7:NICD-P2A-GFP)*. DN-ERBB2 (65224), CA-ERBB2 (16259), and PH-ATK-GFP (51465) plasmids were obtained from Addgene. WT-MYL9-mRuby, CA-MYL9-mRuby, DN-MYL9-mRuby, and full-length zebrafish *actr2b* and *arpin* cDNA, each fused with mRuby (*arpin-mRuby* and *actr2b-mRuby*), were synthesized by Suzhou Genewiz Biotechnology (Suzhou, China). The notch-intracellular domain (NICD) fragment were PCR-amplified from plasmid *hsp70l:loxP-mCherry-stop-loxP-NICD-P2A-Emerald* (*42*). DNA fragments were incorporated into a vector containing the zebrafish *myl7* promoter. Subsequently, 25 to 50 pg of plasmid DNA and *tol2* mRNA were coinjected into one-cell stage embryos. F_0 embryos

exhibiting GFP, mCherry, or mRuby fluorescence were raised to adulthood and outcrossed with wild-type fish to screen for the F_1 generation.

Other transgenic lines used in this study are as follows: *Tg(myl7:mCherry)*^{sd7}; *Tg(myl7:memGFP)*; *Tg(kdrl:mCherry)*^{is5}; *Tg(myl7:H2A-mCherry)*^{sd12}; *Tg(5xUAS:EGFP)*^{zf82}, abbreviated as *Tg(UAS:GFP)*; *Tg(5xUAS:RFP)*^{zf83}, abbreviated as *Tg(UAS:RFP)*; *Tg(UAS:Kaede)*^{s1999t}; *Tg(myl7:mVenus-Gmnn)*^{ncv4324}; *Tg(EPV.Tp1-Mmu.Hbb:d2GFP)*^{mw43}, abbreviated as *Tg(Tp1:d2GFP)*; *Tg(β-actin2:loxP-BFP-STOP-loxP-DsRed)*^{sd27}, abbreviated as *Tg(β-act2:BSR)*; and *Tg(BREAAVmlp:d2GFP)*^{mw30}, abbreviated as *Tg(BRE:d2GFP)*.

Single-cell RNA sequencing and data processing

To prepare the single-cell suspension, approximately 500 hearts were dissected from transgenic *myl7:mCherry* larvae at 72 hpf, following established procedures (*43*). The hearts were then dissociated using 0.25% trypsin (Gibco, USA) and 0.2% collagenase type I (Gibco, USA) for 30 min at 37°C, with intermittent pipetting to ensure complete dissociation. The samples were filtered through a 40-μm cell strainer, followed by centrifugation at 800 g for 5 min, and the supernatant was discarded. The cell pellet was resuspended in red blood cell lysis buffer (MACS, Germany) and incubated for 10 min. After another round of centrifugation, the supernatant was removed, and the cell pellet was resuspended in RPMI 1640 (Corning, USA) containing 0.04% bovine serum albumin (BSA; MACS, Germany). Subsequently, the single-cell suspensions were loaded onto a Chromium Single Cell Controller Instrument (10× Genomics, USA) to generate single-cell gel beads in emulsions. Reverse transcription, cDNA PCR amplification, and library preparation were then performed following the manufacturer's instructions. All libraries were sequenced using the Illumina NovaSeq 6000 with 2 × 150 bp paired-end reads.

Raw sequencing reads were processed and aligned to the zebrafish reference transcriptome (GRCz11) using Cell Ranger version 3.0.2. Subsequently, the R package Seurat (version 4.0.2) was applied to perform downstream analysis with appropriate parameters as previously described (*44*). Visualization of all clusters in two dimensions was achieved using Uniform Manifold Approximation and Projection (UMAP) or t-distributed stochastic neighbor embedding. These clusters were annotated on the basis of the presence of differentially expressed markers within each cluster or through comparison with published single-cell datasets.

RNAscope analysis

Whole-mount labeling of *erbb2* in *erbb2:Gal4;UAS:GFP* zebrafish embryos was performed using an RNAscope probe and the Multiplex Fluorescent Detection Kit version 2 [Advanced Cell Diagnostics (ACD), 323100], according to the manufacturer's protocol. In brief, 96 hpf zebrafish larvae were anesthetized and fixed overnight at room temperature in 10% neutral buffered formalin (NBF). After a 10-min wash in PBST [0.3% Triton X-100 in phosphate-buffered saline (PBS)], larvae were gradually dehydrated in PBST-methanol solutions (10 min per step) and stored at −20°C overnight. Samples were then rehydrated stepwise from 100% methanol to PBST, treated with prewarmed 1X Target Retrieval solution (ACD), and incubated for 6 min in a 100°C heat block. Embryos were then immediately washed for 1 min in 1 ml of PBST + 1% BSA (PBST-BSA), followed by 1 min in methanol and 10 min in PBST-BSA. After rehydration, larvae were fixed in 10% NBF for 25 min, followed by a 10-min wash in PBST-BSA. Next, PBST-BSA buffer was replaced with three drops of Protease Plus (ACD), and samples were incubated for 10 min in a 40°C metal bath, followed by a 10-min wash in PBST-BSA. Embryos were rinsed in three drops of prewarmed probe diluent (ACD) and incubated overnight in the dark with 300 μl RNAscope Probe-Dr-*erbb2*-C2 (ACD, 593001-C2, 1:50 dilution) in a 40°C heat block. For AMPs 1-3, HRP C1-C3, and the HRP blocker (ACD), three drops of each solution were sequentially added after removing the previous solution. TSA Vivid Fluorophore 570 for HRP probe conjugation was diluted 1:1000 in TSA buffer (ACD) for fluorescence labeling. Last, embryos were washed twice for 10 min in PBST and incubated in block solution (10% normal goat serum, 1% BSA, and 0.3% Triton X-100 in PBS) for 1 hour. Primary mouse anti-GFP antibody (Santa Cruz, 1:100 dilution) was diluted in block solution, and embryos were incubated with the primary antibody at 4°C for 24 hours. Samples were washed three times for 10 min in PBST and then incubated with goat anti-mouse immunoglobulin G (IgG; H + L) cross-adsorbed secondary antibody, Alexa Fluor 488 (Invitrogen, A-11001, 1:400 dilution) overnight at 4°C in the dark. Last, whole mount–labeled embryos were washed and mounted in 1% low-melting agarose for confocal imaging.

Immunofluorescence

We conducted whole-mount immunofluorescence staining on zebrafish embryos and adult hearts following previously described protocols (*6*, *45*). The larvae were anesthetized and fixed overnight in 4% paraformaldehyde (Biosharp), then washed three times with PBS containing 0.1% Tween-20 (PBST). Following gradient dehydration and rehydration, the samples were permeabilized with proteinase K (Sigma-Aldrich) in PBST for 20 min and blocked in PBST containing 10% goat serum (Beyotime). Embryos were then incubated overnight at 4°C with gentle shaking in PBST containing the following antibodies: phosphorylated myosin regulatory light chain (Ser19) antibody (Abcam ab2480, 1:100 dilution), anti-Arp2 antibody (Santa Cruz Biotechnology, sc-166103), and anti-Arp3 antibody (Santa Cruz Biotechnology, sc-48344). Following washing in PBST, embryos were incubated with goat anti-rabbit IgG (H + L) cross-adsorbed secondary antibody, Alexa Fluor 555 (Invitrogen, A-21428, 1:200 dilution) or goat anti-mouse IgG (H + L) cross-adsorbed secondary antibody, Alexa Fluor 555 (Invitrogen, A-21422, 1:200 dilution) for 2 hours in the dark at room temperature. To visualize F-actin, fixed embryos were washed with PBST three times and then incubated with fluorescein isothiocyanate phalloidin (Servicebio, G1028, 1:200 dilution) or tetramethyl rhodamine isothiocyanate phalloidin (Servicebio, G1041, 1:200 dilution) for 2 hours in the dark at room temperature. Last, the samples were washed and mounted in 1% low-melting agarose for imaging.

In toto live imaging of beating hearts

To visualize the dynamic delamination of cardiomyocytes, we used a vertical, dual-side illumination light-sheet microscope with an integrated embryo culture module, as previously described (*21*). The embryos were anesthetized and embedded in 2.25% low-melting agarose (Sangon Biotech) containing tricaine (0.0003%, w/v, Sigma-Aldrich) to maintain a heart rate of approximately 120 beats per minute without affecting cardiac activity at 60 hpf. The V-slot hollow cylinder, housing the embryos, was affixed to a customized titanium stage within the imaging chamber. The chamber was then filled with 0.3× Danieau's buffer supplemented with 0.0045% *N*-phenylthiourea

(PTU; Sigma-Aldrich) and 0.0003% tricaine and maintained at 28°C to ensure the optimal development during imaging. Embryos were maintained in their original positions to eliminate the deviations during the development and imaging.

For in toto live imaging, 561- and 488-nm laser beams were combined and coupled into a single-mode fiber (Thorlabs), which is connected to a collimator (Thorlabs) to minimize the chromatic aberration. The sheet-like laser was made of an achromatic cylindrical lens (Edmund Scientific), which only collimated laser in the *z* direction. To obtain three-dimensional (3D) images at single-cell resolution, a galvo scanning mirror (Cambridge Technologies) was placed in the focal plane of the cylindrical lens to rapidly scan the laser at *z* axis. The galvo was coordinated with the piezoelectric stage of the detection objective to maintain focus during rapid volumetric imaging.

Raw data were subjected to the spatiotemporal alignment using the image frame module to remove positional bias and ensure accuracy in the subsequent analysis. Initial data obtained from the TGMM automatic cell segmentation and tracking system were imported into the Fiji plugin, MaMuT, for manual refinement of navigation, cell segmentation, tracking, and lineage correction to achieve the standard of manual marking (*46*–*48*). Outputs from MaMuT, encompassing cell ID, spatial location, time point index, and lineage information, were the compiled into a MATLAB table for data analysis.

Photoconversion and FRAP experiments

In the photoactivation experiments, PAGFP mRNA was injected into one-cell-stage *erbb2:RFP;*β*-act2:BSR* embryos. At 60 hpf, embryos were mounted in 1% low-melting agarose containing tricaine (1 mg/ml; Sigma-Aldrich) to halt cardiac contraction before imaging. Individual *erbb2:RFP*$^{+}$ or *erbb2:RFP*$^{-}$ cardiomyocytes was then photoactivated using a 405-nm laser at 50% laser power for 2 s. Subsequently, the embryos were removed from the agarose, resuscitated, and incubated in 0.3× Danieau's buffer for an additional 20 hours before image acquisition. For Kaede photoconversion, a single cardiomyocyte in *erbb2:Kaede;*β*-act2:BSR* embryos was illuminated with a 405-nm laser at 50% laser power for 2 s. Subsequently, embryos were cultured in 0.3× Danieau's buffer and imaged at 80 hpf using a confocal microscope.

We conducted FRAP analysis on *erbb2:GFP;myl7:WT-MYL9-mRuby* fish using a Nikon C2 confocal microscope coupled with a 20× objective. Initially, we identified either *erbb2:GFP*$^{+}$ or *erbb2:GFP*$^{-}$ cardiomyocyte before selecting a region of interest (ROI) within individual cells. This ROI was then photobleached using a 405-nm laser at 50% laser power for 20 to 25 iterations. Following photobleaching, consecutive image frames were captured to monitor fluorescence recovery. ROI analysis at the bleached area was performed using Fiji software, with the mean intensity values at each time point normalized to the average prebleach values (GraphPad Prism 9).

Clonal analysis

Cardiomyocyte clones were genetically labeled using the *tol2*-mediated zebrafish transgenesis strategy. In brief, individual plasmid (25 to 50 pg) and *tol2* mRNA were coinjected into embryos at the one-cell stage to generate mosaic hearts. Embryos were maintained in 0.3× Danieau's buffer and treated with 0.0045% PTU (Sigma-Aldrich) starting at 24 hpf to prevent pigmentation. Confocal imaging was performed on the mosaic hearts after fluorescence screening or inhibitory treatment at the indicated stages.

Small-molecule treatments

Embryos were cultured in 0.3× Danieau's buffer supplemented with 0.0045% PTU at 24 hpf to prevent pigmentation. Before chemical treatment, embryos were dechorionated and screened for fluorescence using a stereoscopic microscope. Zebrafish larvae were incubated in 10 μM PD168393 (MCE) or 5 μM AG1478 (Merck) at 60 hpf to inhibit Erbb2 signaling (*6*, *15*). Alfacalcidol (7 μM, Selleck) was added at specific developmental stages to stimulate cardiomyocyte proliferation (*27*). PI3K activity was inhibited using LY294002 (20 μM, Sigma-Aldrich), and the Arp2/3 complex was targeted with CK666 (25 μM, Sigma-Aldrich). A modified combination of jasplakinolide (0.8 μM, Sigma-Aldrich), latrunculin A (0.125 μM, Sigma-Aldrich), and Y27632 (1 μM, Sigma-Aldrich), collectively referred to as "JLY," was used to decouple PI3K signaling from its regulation of actin dynamics (*31*). To suppress Notch activity, embryos were treated with 100 μM DAPT (Sigma-Aldrich) during the 60- to 72-hpf or 84- to 96-hpf intervals (*49*). All chemicals were prepared in DMSO to generate stock solutions, with DMSO also serving as the vehicle control for comparisons.

Cardiac contractility analysis

Embryos were embedded in 1% low-melting agarose containing 0.004% tricaine at the indicated stages. Time-lapse images of transgenic zebrafish hearts were recorded for 1 min using a Nikon Ti2 microscope at 25 frames per second. Cardiac contractility was calculated using fractional area change analysis: Fractional area change (%) = $(\text{Area}_{\text{diastole}} - \text{Area}_{\text{systole}}) / \text{Area}_{\text{diastole}} \times 100\%$.

RNA-sequencing analysis

Embryonic hearts from DAPT- or DMSO-treated *myl7:mCherry* transgenic fish were isolated and purified following established procedures (*43*). Total RNA was extracted using TRIzol (Ambion), and 1 μg of RNA per sample was used as a replicate for RNA sequencing. The transcriptome library construction and bulk RNA sequencing were conducted by the Beijing Genomics Institute on an Illumina HiSeq 2500 system. Raw sequencing reads were aligned to the zebrafish reference genome (GRCz11) using STAR version 2.7.1a. Gene expression counts for each sample were calculated with featureCounts version 1.6.0, retaining genes with more than 0.5 counts per million reads. Differential gene expression analysis was carried out using the glmLRT method implemented in edgeR, with a P value < 0.05 indicating significance. GSEA was performed using clusterProfiler.

Quantitative RT-PCR

Reverse transcription was conducted using Perfect Real Time Primescript RT reagent (Takara, RR047A) following the manufacturer's protocol. qRT-PCR was performed in an optical 384-well plate using the LightCycler Real-Time PCR System (Roche) and TB Green Premix Ex Taq (Takara, RR430A), with each assay conducted in triplicate. The qRT-PCR conditions were set as follows: an initial denaturation step at 95°C for 30 s, followed by 40 amplification cycles of 5 s at 95°C, and 30 s at 60°C. Primer specificity was verified through melting curve analysis. The relative mRNA levels were normalized to *actb1* mRNA, serving as the internal control. Sequences of qRT-PCR primers are as follows: *actb1* Forward, 5′-ACCACGGCCGAAAGAGAAAT-3′; and Reverse 5′-GCAAGATTCCATACCCAGGA-3′; and *erbb2* Forward, 5′-GTCGGTGGAGTGCTTCTCTTCATC-3′; and Reverse, 5′-TCGTGCTCCTGTAGGCGTCTC-3′.

Image processing and statistical analysis

Confocal images were acquired using a Nikon C2 microscope coupled with a 20× objective. To analyze the subcellular localization of p-myo, F-actin, and PH-AKT, we generated fluorescence intensity profiles along the apical-basal axis of individual cardiomyocytes. For comprehensive visualization of cardiac structure, we performed 3D reconstructions and maximum projections of confocal slices using Nikon NIS Elements and Fiji software. The quantification of total cardiomyocytes and clones within the ventricle was based on these 3D reconstructions. To measure the number of trabeculae in each heart, cardiomyocytes within the compact layer were delineated in individual confocal slices based on their spatial location and then manually masked. Using these masked slices, 3D reconstructions allowed the exclusive measurement of trabeculae. Quantification of cardiomyocytes in the compact layer were calculated by subtracting trabecular cardiomyocyte counts from the total. To standardize the analyses of trabeculation, we focused on the outer curvature of the ventricles, where most trabeculae formation occurs. Different batches of embryos were collected on different days. All experiments were repeated independently for at least three times, and the sample sizes were not predetermined. Statistical analyses were conducted using GraphPad Prism 9. The distribution of each sample group was assessed using the D'Agostino-Pearson test. For data that followed a normal distribution, parametric tests were used: a two-tailed Student's *t* test for comparisons between two samples or one-way analysis of variance (ANOVA) for multiple group comparisons. For data that were not normally distributed, we performed nonparametric tests: a two-tailed Mann-Whitney *U* test for comparisons between two samples or a Kruskal-Wallis test for multiple group comparisons. $P < 0.05$ indicating statistical significance and denoted by an asterisk. Error bars in figures represent SEM.

Supplementary Materials

The PDF file includes:

Figs. S1 to S12
Tables S1 and S2
Legend for movie S1
Legend for dataset S1

Other Supplementary Material for this manuscript includes the following:

Movie S1
Dataset S1

REFERENCES AND NOTES

1. Y. Mao, S. A. Wickström, Mechanical state transitions in the regulation of tissue form and function. *Nat. Rev. Mol. Cell Biol.* **25**, 654–670 (2024).
2. C. Villeneuve, A. Hashmi, I. Ylivinkka, E. Lawson-Keister, Y. A. Miroshnikova, C. Pérez-González, S.-M. Myllymäki, F. Bertillot, B. Yadav, T. Zhang, D. Matic Vignjevic, M. L. Mikkola, M. L. Manning, S. A. Wickström, Mechanical forces across compartments coordinate cell shape and fate transitions to generate tissue architecture. *Nat. Cell Biol.* **26**, 207–218 (2024).
3. N. Mishra, C.-P. Heisenberg, Dissecting organismal morphogenesis by bridging genetics and biophysics. *Annu. Rev. Genet.* **55**, 209–233 (2021).
4. V. Gupta, K. D. Poss, Clonally dominant cardiomyocytes direct heart morphogenesis. *Nature* **484**, 479–484 (2012).
5. D. W. Staudt, J. Liu, K. S. Thorn, N. Stuurman, M. Liebling, D. Y. Stainier, High-resolution imaging of cardiomyocyte behavior reveals two distinct steps in ventricular trabeculation. *Development* **141**, 585–593 (2014).
6. P. Han, J. Bloomekatz, J. Ren, R. Zhang, J. D. Grinstein, L. Zhao, C. G. Burns, C. E. Burns, R. M. Anderson, N. C. Chi, Coordinating cardiomyocyte interactions to direct ventricular chamber morphogenesis. *Nature* **534**, 700–704 (2016).
7. A. F. Moorman, V. M. Christoffels, Cardiac chamber formation: Development, genes, and evolution. *Physiol. Rev.* **83**, 1223–1267 (2003).
8. M. H. Dominguez, A. L. Krup, J. M. Muncie, B. G. Bruneau, Graded mesoderm assembly governs cell fate and morphogenesis of the early mammalian heart. *Cell* **186**, 479–496. e423 (2023).
9. P. Sidhwani, D. Yelon, Fluid forces shape the embryonic heart: Insights from zebrafish. *Curr. Top. Dev. Biol.* **132**, 395–416 (2019).
10. M. Gassmann, F. Casagranda, D. Orioli, H. Simon, C. Lai, R. Klein, G. Lemke, Aberrant neural and cardiac development in mice lacking the ErbB4 neuregulin receptor. *Nature* **378**, 390–394 (1995).
11. K. F. Lee, H. Simon, H. Chen, B. Bates, M. C. Hung, C. Hauser, Requirement for neuregulin receptor erbB2 in neural and cardiac development. *Nature* **378**, 394–398 (1995).
12. D. Meyer, C. Birchmeier, Multiple essential functions of neuregulin in development. *Nature* **378**, 386–390 (1995).
13. R. Kramer, N. Bucay, D. J. Kane, L. E. Martin, J. E. Tarpley, L. E. Theill, Neuregulins with an Ig-like domain are essential for mouse myocardial and neuronal development. *Proc. Natl. Acad. Sci. U.S.A.* **93**, 4833–4838 (1996).
14. S. A. Crone, Y. Y. Zhao, L. Fan, Y. Gu, S. Minamisawa, Y. Liu, K. L. Peterson, J. Chen, R. Kahn, G. Condorelli, J. Ross Jr., K. R. Chien, K. F. Lee, ErbB2 is essential in the prevention of dilated cardiomyopathy. *Nat. Med.* **8**, 459–465 (2002).
15. R. Priya, S. Allanki, A. Gentile, S. Mansingh, V. Uribe, H.-M. Maischein, D. Y. R. Stainier, Tension heterogeneity directs form and fate to pattern the myocardial wall. *Nature* **588**, 130–134 (2020).
16. H. Honkoop, D. E. de Bakker, A. Aharonov, F. Kruse, A. Shakked, P. D. Nguyen, C. de Heus, L. Garric, M. J. Muraro, A. Shoffner, F. Tessadori, J. C. Peterson, W. Noort, A. Bertozzi, G. Weidinger, G. Posthuma, D. Grün, W. J. van der Laarse, J. Klumperman, R. T. Jaspers, K. D. Poss, A. van Oudenaarden, E. Tzahor, J. Bakkers, Single-cell analysis uncovers that metabolic reprogramming by ErbB2 signaling is essential for cardiomyocyte proliferation in the regenerating heart. *eLife* **8**, e50163 (2019).
17. R. P. Harvey, Patterning the vertebrate heart. *Nat. Rev. Genet.* **3**, 544–556 (2002).
18. J. Liu, M. Bressan, D. Hassel, J. Huisken, D. Staudt, K. Kikuchi, K. D. Poss, T. Mikawa, D. Y. Stainier, A dual role for ErbB2 signaling in cardiac trabeculation. *Development* **137**, 3867–3875 (2010).
19. G. H. Patterson, J. Lippincott-Schwartz, A photoactivatable GFP for selective photolabeling of proteins and cells. *Science* **297**, 1873–1877 (2002).
20. E. K. Scott, L. Mason, A. B. Arrenberg, L. Ziv, N. J. Gosse, T. Xiao, N. C. Chi, K. Asakawa, K. Kawakami, H. Baier, Targeting neural circuitry in zebrafish using GAL4 enhancer trapping. *Nat. Methods* **4**, 323–326 (2007).
21. Y. Yue, W. Zong, X. Li, J. Li, Y. Zhang, R. Wu, Y. Liu, J. Cui, Q. Wang, Y. Bian, X. Yu, Y. Liu, G. Tan, Y. Zhang, G. Zhao, B. Zhou, L. Chen, W. Xiao, H. Cheng, A. He, Long-term, in toto live imaging of cardiomyocyte behaviour during mouse ventricle chamber formation at single-cell resolution. *Nat. Cell Biol.* **22**, 332–340 (2020).
22. A. Citri, Y. Yarden, EGF-ERBB signalling: Towards the systems level. *Nat. Rev. Mol. Cell Biol.* **7**, 505–516 (2006).
23. O. Kashles, Y. Yarden, R. Fischer, A. Ullrich, J. Schlessinger, A dominant negative mutation suppresses the function of normal epidermal growth factor receptors by heterodimerization. *Mol. Cell. Biol.* **11**, 1454–1463 (1991).
24. S. Reischauer, R. Arnaout, R. Ramadass, D. Y. Stainier, Actin binding GFP allows 4D in vivo imaging of myofilament dynamics in the zebrafish heart and the identification of Erbb2 signaling as a remodeling factor of myofibril architecture. *Circ. Res.* **115**, 845–856 (2014).
25. J. R. Beach, L. S. Licate, J. F. Crish, T. T. Egelhoff, Analysis of the role of Ser1/Ser2/Thr9 phosphorylation on myosin II assembly and function in live cells. *BMC Cell Biol.* **12**, 52 (2011).
26. W. Y. Choi, M. Gemberling, J. Wang, J. E. Holdway, M. C. Shen, R. O. Karlstrom, K. D. Poss, In vivo monitoring of cardiomyocyte proliferation to identify chemical modifiers of heart regeneration. *Development* **140**, 660–666 (2013).
27. Y. Han, A. Chen, K. B. Umansky, K. A. Oonk, W. Y. Choi, A. L. Dickson, J. Ou, V. Cigliola, O. Yifa, J. Cao, V. A. Tornini, B. D. Cox, E. Tzahor, K. D. Poss, Vitamin D stimulates cardiomyocyte proliferation and controls organ size and regeneration in zebrafish. *Dev. Cell* **48**, 853–863.e5 (2019).
28. M. A. Lemmon, J. Schlessinger, Cell signaling by receptor tyrosine kinases. *Cell* **141**, 1117–1134 (2010).
29. M. P. Scheid, J. R. Woodgett, PKB/AKT: Functional insights from genetic models. *Nat. Rev. Mol. Cell Biol.* **2**, 760–768 (2001).
30. T. F. Franke, D. R. Kaplan, L. C. Cantley, A. Toker, Direct regulation of the Akt proto-oncogene product by phosphatidylinositol-3,4-bisphosphate. *Science* **275**, 665–668 (1997).
31. N. M. Neumann, M. C. Perrone, J. H. Veldhuis, R. J. Huebner, H. Zhan, P. N. Devreotes, G. W. Brodland, A. J. Ewald, Coordination of receptor tyrosine kinase signaling and interfacial tension dynamics drives radial intercalation and tube elongation. *Dev. Cell* **45**, 67–82.e6 (2018).
32. P. Várnai, T. Balla, Visualization of phosphoinositides that bind pleckstrin homology domains: Calcium- and agonist-induced dynamic changes and relationship to Myo-[3H] inositol-labeled phosphoinositide pools. *J. Cell Biol.* **143**, 501–510 (1998).

33. P. Devreotes, A. R. Horwitz, Signaling networks that regulate cell migration. *Cold Spring Harb. Perspect. Biol.* **7**, a005959 (2015).
34. M. Spillane, A. Ketschek, S. L. Jones, F. Korobova, B. Marsick, L. Lanier, T. Svitkina, G. Gallo, The actin nucleating Arp2/3 complex contributes to the formation of axonal filopodia and branches through the regulation of actin patch precursors to filopodia. *Dev. Neurobiol.* **71**, 747–758 (2011).
35. I. Dang, R. Gorelik, C. Sousa-Blin, E. Derivery, C. Guérin, J. Linkner, M. Nemethova, J. G. Dumortier, F. A. Giger, T. A. Chipysheva, V. D. Ermilova, S. Vacher, V. Campanacci, I. Herrada, A. G. Planson, S. Fetics, V. Henriot, V. David, K. Oguievetskaia, G. Lakisic, F. Pierre, A. Steffen, A. Boyreau, N. Peyriéras, K. Rottner, S. Zinn-Justin, J. Cherfils, I. Bièche, A. Y. Alexandrova, N. B. David, J. V. Small, J. Faix, L. Blanchoin, A. Gautreau, Inhibitory signalling to the Arp2/3 complex steers cell migration. *Nature* **503**, 281–284 (2013).
36. A. L. Duchemin, H. Vignes, J. Vermot, R. Chow, Mechanotransduction in cardiovascular morphogenesis and tissue engineering. *Curr. Opin. Genet. Dev.* **57**, 106–116 (2019).
37. S. Abdul-Wajid, B. L. Demarest, H. J. Yost, Loss of embryonic neural crest derived cardiomyocytes causes adult onset hypertrophic cardiomyopathy in zebrafish. *Nat. Commun.* **9**, 4603 (2018).
38. Y. Zhou, T. J. Cashman, K. R. Nevis, P. Obregon, S. A. Carney, Y. Liu, A. Gu, C. Mosimann, S. Sondalle, R. E. Peterson, W. Heideman, C. E. Burns, C. G. Burns, Latent TGF-β binding protein 3 identifies a second heart field in zebrafish. *Nature* **474**, 645–648 (2011).
39. J. Li, B. B. Zhang, Y. G. Ren, S. Y. Gu, Y. H. Xiang, J. L. Du, Intron targeting-mediated and endogenous gene integrity-maintaining knockin in zebrafish using the CRISPR/Cas9 system. *Cell Res.* **25**, 634–637 (2015).
40. D. Liu, Z. Wang, A. Xiao, Y. Zhang, W. Li, Y. Zu, S. Yao, S. Lin, B. Zhang, Efficient gene targeting in zebrafish mediated by a zebrafish-codon-optimized Cas9 and evaluation of off-targeting effect. *J. Genet. Genomics* **41**, 43–46 (2014).
41. N. Chang, C. Sun, L. Gao, D. Zhu, X. Xu, X. Zhu, J. W. Xiong, J. J. Xi, Genome editing with RNA-guided Cas9 nuclease in zebrafish embryos. *Cell Res.* **23**, 465–472 (2013).
42. R. M. Anderson, M. Delous, J. A. Bosch, L. Ye, M. A. Robertson, D. Hesselson, D. Y. R. Stainier, M. C. Mullins, Hepatocyte growth factor signaling in intrapancreatic ductal cells drives pancreatic morphogenesis. *PLOS Genet.* **9**, e1003650 (2013).
43. C. G. Burns, C. A. MacRae, Purification of hearts from zebrafish embryos. *Biotechniques* **40**, https://pubmed.ncbi.nlm.nih.gov/1656881X6/ (2006).
44. A. Butler, P. Hoffman, P. Smibert, E. Papalexi, R. Satija, Integrating single-cell transcriptomic data across different conditions, technologies, and species. *Nat. Biotechnol.* **36**, 411–420 (2018).
45. P. Han, X. H. Zhou, N. Chang, C. L. Xiao, S. Yan, H. Ren, X. Z. Yang, M. L. Zhang, Q. Wu, B. Tang, J. P. Diao, X. Zhu, C. Zhang, C. Y. Li, H. Cheng, J. W. Xiong, Hydrogen peroxide primes heart regeneration with a derepression mechanism. *Cell Res.* **24**, 1091–1107 (2014).
46. F. Amat, W. Lemon, D. P. Mossing, K. McDole, Y. Wan, K. Branson, E. W. Myers, P. J. Keller, Fast, accurate reconstruction of cell lineages from large-scale fluorescence microscopy data. *Nat. Methods* **11**, 951–958 (2014).
47. J. Schindelin, I. Arganda-Carreras, E. Frise, V. Kaynig, M. Longair, T. Pietzsch, S. Preibisch, C. Rueden, S. Saalfeld, B. Schmid, J. Y. Tinevez, D. J. White, V. Hartenstein, K. Eliceiri, P. Tomancak, A. Cardona, Fiji: An open-source platform for biological-image analysis. *Nat. Methods* **9**, 676–682 (2012).
48. K. Jaqaman, D. Loerke, M. Mettlen, H. Kuwata, S. Grinstein, S. L. Schmid, G. Danuser, Robust single-particle tracking in live-cell time-lapse sequences. *Nat. Methods* **5**, 695–702 (2008).
49. R. Zhang, P. Han, H. Yang, K. Ouyang, D. Lee, Y. F. Lin, K. Ocorr, G. Kang, J. Chen, D. Y. Stainier, D. Yelon, N. C. Chi, In vivo cardiac reprogramming contributes to zebrafish heart regeneration. *Nature* **498**, 497–501 (2013).

Acknowledgments: We thank Y. Han for providing the *Tg(myl7:mVenus-Gmnn)* line. We also thank Y. Li from the Core Facilities, Zhejiang University School of Medicine for the technical support. **Funding:** This work was supported by the National Key R&D Program of China (2023YFA1800600 and 2018YFA0800501), the National Natural Science Foundation of China (32170823, 92468104, and 31871462) to P.H., and the Youth Innovation Promotion Association of Chinese Academy of Sciences to J.Li. **Author contributions:** Conceptualization: P.H., J.L., and S.C. Methodology: P.H., J.L., J.Li., P.J., S.Y., S.C., and A.H. Investigation: J.L., P.J., J.Li., and P.H. Visualization: J.L., S.C., J.Li., and P.H. Formal analysis: P.H., J.L., S.Y., K.X., and T.C. Supervision: P.H., J.Li., A.H., J.-W.X., and P.X. Writing–original draft: J.L., P.H., J.Li., and T.C. Writing–review and editing: P.H. and J.L. **Competing interests:** The authors declare that they have no competing interests. **Data and materials availability:** All data needed to evaluate the conclusions in the paper are present in the paper and/or the Supplementary Materials. The single-cell RNA-seq datasets are available from Gene Expression Omnibus (GEO) under the accession number GSE261718. The single-cell RNA-seq datasets of zebrafish heart at 48 hpf were obtained from published study in GEO under the accession code GSE139218. The raw RNA-sequencing data have been deposited in the GEO database with the accession number GSE261479.

Submitted 8 August 2024
Accepted 3 February 2025
Published 7 March 2025
10.1126/sciadv.ads2998